Resonant Raman scattering in self-assembled quantum dots

E. Menéndez-Proupin and C. Trallero-Giner

Department of Theoretical Physics, Havana University, Vedado 10400, Havana, Cuba

S. E. Ulloa

Department of Physics and Astronomy and Condensed Matter and Surface Sciences Program, Ohio University, Athens, Ohio 45701-2979

(Received 15 July 1999)

A theoretical treatment for first-order resonant Raman scattering in self-assembled quantum dots (SAQD's) of different materials is presented. The dots are modeled as cylindrical disks with elliptical cross section, to simulate shape and confinement anisotropies obtained from the SAQD growth conditions. Coulomb interaction between electron and hole is considered in an envelope function Hamiltonian approach and the eigenvalues and eigenfunctions are obtained by a matrix diagonalization technique. By including excitonic intermediate states in the Raman process, the scattering efficiency and cross section are calculated for long-range Fröhlich exciton-phonon interaction. The Fröhlich interaction in the SAQD is considered in an approach in which both the mechanical and electrostatic matching boundary conditions are fulfilled at the SAQD interfaces. Exciton and confined phonon selection rules are derived for Raman processes. Characteristic results for SAQD's are presented, including InAs dots in GaAs, as well as CdSe dots in ZnSe substrates. We analyze how Raman spectroscopy would give information on carrier masses, confinement anisotropy effects, and SAQD geometry. [S0163-1829(99)16847-4]

I. INTRODUCTION

Self-assembled quantum dots (SAQD's), produced by clever flux interruption and control of growth conditions in molecular beam epitaxy chambers, have been vigorously studied over the last few years.[1] These semiconductor structures are characterized by the strong quantum confinement of charge carriers they provide, given their nanometer dimensions. Either by photoproduction, nearby doping, or tunneling into micron-size capacitance arrangements,[2] electrons and/or holes introduced into these structures experience the strong local potential provided by structural constraints, applied gate voltages, as well as by long-ranged strain fields. The effective confinement potential includes the combined effect of structural and electrostatic potentials, as well as lattice and strain anisotropies, and may have, in general, quite a complicated symmetry. Since several growth techniques and conditions are employed to fabricate SAQD's, the resulting geometries and sample configurations yield a variety of different structures.[1]

It is experimentally clear that SAQD's shapes vary over a wide range, from well-facetted pyramids,[3] to smoother flat lenticular shapes,[1] depending critically on growth and local environment conditions, as well as thermal treatment and regrowth of the substrate material. Photoluminescence (PL) and photoluminescence excitation (PLE) experiments are routinely used to provide information on the overall size of the resulting SAQD's, since due to the carrier confinement there is a direct correlation between decreasing sizes and a larger blueshift of the PL signal. Mapping of the quantum dot shape is also accomplished by a variety of microscopy techniques, from transmission electron microscopy (TEM) to atomic force microscopy (AFM) and scanning tunneling microscopy (STM), but quantitative and detailed information on the effective potential in a given structure is difficult to obtain. As in many other problems, it is always desirable to have alternative characterization techniques which yield complementary information. Raman scattering provides just such alternatives, as we will describe here, because of its sensitivity to structural parameters of the system.

We should emphasize that a large number of interesting experimental results have already appeared in the literature, where the SAQD's are characterized by PL and PLE.[1] However, recent work by several groups has yielded interesting first results of Raman scattering in these systems. In these works, light scattering has been used to characterize possible intermixing of materials upon deposition or as a consequence of thermal treatment,[4] and to study the shifting of interface modes due to strain.[5] Similarly, an exploration of optical and acoustic phonons in quantum dots embedded in a waveguide was presented in Ref. 6. In these works, however, no analysis is made of the intervening electronic (or excitonic) states, perhaps due to the lack of a specific model to compare these experiments against. One should mention, however, that a preliminary analysis of the role of electronic states in the inelastic light scattering was carried out by Hawrylak *et al.*, with a successful qualitative comparison.[7]

In this paper, we present a theoretical treatment of the resonant Raman scattering by confined phonons in SAQD's. By full incorporation of the elements entering these experiments, namely the effects of the effective potential on excitonic states, the LO-phonon dispersion for modes confined in the dot, and a detailed calculation of the various matrix elements involved in the Fröhlich coupling, we provide the basis for quantitative analysis of Raman experiments in these systems. For concreteness, we focus our attention here on a model of asymmetric dot confinement, where the effective potential is assumed to be that of a cylindrical pill box with elliptical cross section, and we study the effects of this noncircular geometry on the *inelastic light scattering* and optical
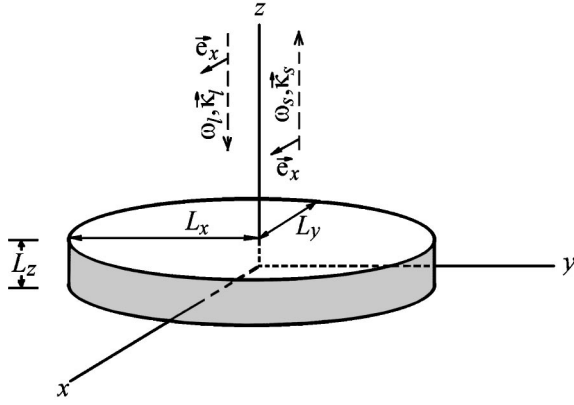
FIG. 1. A schematic picture of the self-organized quantum dot modeled as a quantum disk with an elliptical shape in the XY plane and height L_z. The Raman backscattering configuration along the $Z\|[001]$ direction is shown. Lateral confinement is harmoniclike, with $L_{x/y} = \sqrt{\hbar/\mu\omega_{x/y}}$.

response. We find that the elliptical symmetry has strong and clear signatures in the light scattering cross section, as well as in PL and PLE. Moreover, we show that detailed analysis of the Raman coupling could give one information on the effective mass of the carriers, since they affect strongly the general features and overall peak distribution and amplitudes of the Raman intensity profiles.

Since the Raman scattering data is expected to be more prevalent in the study of these systems in the near future, and because of its intrinsic interest, we present a detailed analysis of a model for a SAQD which captures the essential physics of the problem. In fact, the cylindrical box model is likely to be a good model of rather flattened nonfacetted dots, where the characteristic dimensions are 3 nm in height and 28 nm in diameter,[4] for example. Similarly large diameter/height aspect ratios are typical in these systems and our model should provide a good description.

The remainder of the paper is organized as follows. Section II will develop the theory for Raman resonant scattering (RRS) applied to the case of quantum disks with a large aspect ratio, discussing the nature of the excitonic states in these structures, as well as the matrix elements involving exciton-phonon interaction. Section III develops the expressions for the Raman polarizability and cross section, and presents results for the InAs/GaAs system, as well as in the CdSe/ZnSe system. Finally, Sec. IV contains conclusions and discussion of results. In the Appendix, we present some technical details of the calculations.

II. THEORY OF RRS IN QUANTUM DISKS

A schematic picture of a short-cylindrical quantum disk with an oblate spheroidal profile is shown in Fig. 1. We assume that the QD is grown along the [001] direction denoted by Z, while the [100] and [010] directions lie along X and Y, respectively. In a backscattering configuration on the [001] surface of cubic semiconductors, the Raman tensor can be written as[8]

$$\vec{R} = \begin{pmatrix} a_F & a_{DP} & 0 \\ a_{DP} & a_F & 0 \\ 0 & 0 & a_F \end{pmatrix}, \quad (1)$$

with a_F and a_{DP} being the Raman polarizability for allowed and forbidden scattering, respectively, at the level of the dipole approximation. The allowed scattering by optical longitudinal phonons in bulk semiconductors is via the deformation potential, while the Fröhlich-like events are forbidden. In this case, the square Raman polarizability is given by[9]

$$|a|^2 = |\mathbf{e}_s \cdot \vec{R} \cdot \mathbf{e}_l|^2 = \sum_f \left| \frac{\eta_l \eta_s}{2\pi} \frac{V_c}{u_0} \frac{1}{\hbar\omega_l} W_{fi}(\omega_s, \mathbf{e}_s; \omega_l, \mathbf{e}_l) \right|^2, \quad (2)$$

where ω_l (ω_s) is the incident (scattered) light frequency with polarization $\mathbf{e}_l$ ($\mathbf{e}_s$) and η_l (η_s) is the corresponding refraction index of the sample, and the sum over final states refers to the different final phonon modes involved in the transition, as we will specify later. V_c is the volume of the primitive cell and u_0 is the relative phonon displacement.[9] For a first-order process the probability amplitude is expressed as

$$W_{fi} = \sum_{\mu_1,\mu_2} \frac{\langle f|H_{E-R}|\mu_2\rangle\langle\mu_2|H_{E-P}|\mu_1\rangle\langle\mu_1|H_{E-R}|i\rangle}{(\hbar\omega_s - E_{\mu_2} + i\Gamma_{\mu_2})(\hbar\omega_l - E_{\mu_1} + i\Gamma_{\mu_1})}. \quad (3)$$

Here, $|\mu_j\rangle$ ($j=1,2$) refers to the excitonic intermediate states in the QD with energy E_{μ_j} and lifetime broadening Γ_{μ_j}. The exciton-radiation interaction can be expressed as[10]

$$H_{E-R} = \sum_{\boldsymbol{\kappa},\mathbf{e},\mu} \{T_{cv}^{\mu} D_{\mu}^{\dagger} a_{\boldsymbol{\kappa},\mathbf{e}} + T_{cv}^{\mu*} D_{\mu} a_{\boldsymbol{\kappa},\mathbf{e}}\} + \text{H.c.}, \quad (4)$$

where $D_{\mu}^{\dagger}$ (D_{μ}) is the creation (annihilation) operator for excitons with quantum number μ and $a_{\boldsymbol{\kappa},\mathbf{e}}$ is the annihilation photon operator with wave vector $\boldsymbol{\kappa}$ and polarization $\mathbf{e}$. T_{cv}^{μ} is the exciton-photon coupling coefficient which for direct allowed transitions between c and v bands and in the electric dipole envelope function approximation takes the form[11]

$$T_{cv}^{\mu} = \frac{e}{m_0}\sqrt{\frac{2\pi\hbar}{V\omega\eta^2}}\mathbf{e}\cdot\mathbf{p}_{cv}\int \Psi_{\mu}^{*}(\mathbf{r}_e=\mathbf{r}_0,\mathbf{r}_h=\mathbf{r}_0)d^3\mathbf{r}_0. \quad (5)$$

Here, $\Psi_{\mu}(\mathbf{r}_e,\mathbf{r}_h)$ is the exciton wave function of the quantum disk and $\mathbf{p}_{cv} = \langle c|\mathbf{p}|v\rangle$ is the interband optical matrix element of the momentum operator between conduction- and valence-band Bloch functions.

We assume that $L_x, L_y \gg L_z$, as observed in typical SAQD samples, which results in the optical phonons being confined on the Z direction, leading to a quantization of the phonon wave vector q_z along the QD axis. In this case, the exciton-phonon interaction can be taken as

$$H_{E-P} = \sum_{\mu_1,\mu_2} S_{\mu_1}^{\mu_2}(\mathbf{q},n) D_{\mu_2}^{\dagger} D_{\mu_1} b_{\mathbf{q},n}^{\dagger} + \text{H.c.}, \quad (6)$$

where $b_{\mathbf{q},n}^{\dagger}$ is the creation operator for a phonon with an in-plane wave vector $\mathbf{q}$ and frequency $\omega_n(\mathbf{q})$. In zinc-blende type semiconductors, and following Eq. (1), the Fröhlich mechanism can be observed in the backscattering configuration $Z(X,X)\bar{Z}$ for a [001] surface. Due to the long wavelength of the optical transitions involved, one can use the dipole approximation (the phonon wave vector is taken to be

zero), and then the Raman process is forbidden in the bulk.[8] However, in semiconductor nanostructures such as quantum wells and QDs the confinement of the phonon makes this scattering process allowed, and the Fröhlich mechanism even becomes the strongest.[12] Considering only the diagonal component of the Raman tensor (1), the expression for the exciton-LO phonon coupling constant is[13]

$$S_{\mu_1}^{\mu_2}(\mathbf{q},n) = \frac{C_F(\omega_L/\omega_n)^{1/2}}{[q^2 + (n\pi/L_z)^2]^{1/2}}$$
$$\times \langle \mu_2 | \Phi_F^{(n)}(z_e)e^{-i\mathbf{q}\cdot\mathbf{r}_e} - \Phi_F^{(n)}(z_h)e^{-i\mathbf{q}\cdot\mathbf{r}_h} | \mu_1 \rangle \quad (7)$$

with

$$\Phi_F^{(n)}(z) = \begin{cases} e^{qz}[e^{qL_z/2} - (-1)^n e^{-qL_z/2}]; & z \le -\dfrac{L_z}{2} \\[2mm] 2\cos\left[\dfrac{n\pi}{L_z}\left(z + \dfrac{L_z}{2}\right)\right]; & -\dfrac{L_z}{2} \le z \le \dfrac{L_z}{2} \\[2mm] e^{-qz}[(-1)^n e^{qL_z/2} - e^{-qL_z/2}]; & z \ge \dfrac{L_z}{2}, \end{cases} \quad (8)$$

$$\omega_n^2(\mathbf{q}) = \omega_L^2 - \beta_L^2\left[\left(\frac{n\pi}{L_z}\right)^2 + q^2\right]; \quad n = 1,2,\ldots, \quad (9)$$

and

$$C_F = -ie\left[\frac{2\pi\hbar\omega_L}{V}(\varepsilon_\infty^{-1} - \varepsilon_0^{-1})\right]^{1/2}. \quad (10)$$

In these expressions, ω_L and β_L describe the quadratic LO-phonon dispersion in the bulk semiconductor, while ε_0 and ε_∞ are the static and optical dielectric constants, respectively. The above equations include the confinement of the phonon wave function and resulting eigenfrequencies along the Z axis. The phonon wave vector is then described by a perpendicular component $\mathbf{q}$ to the SAQD growth (Z axis) direction, and a parallel q_z component (quantized due to the confinement in the quantum disk). For the backscattering configuration shown in Fig. 1, only LO vibrations with $q_z = n\pi/L_z$ (with $n = 1,2,\ldots$), and $\mathbf{q} = 0$ are allowed to participate.[12] We should notice that the Fröhlich potential (8) is only valid in the limit $\mathbf{q} \approx 0$, where the coupling between the longitudinal and transverse polarization modes, which appears as a consequence of the matching boundary conditions, can be disregarded. The electron-phonon interaction (8) satisfies the electrostatic boundary conditions (continuity of the electrostatic potential and the Z component of vector displacement field) as well as the mechanical boundary conditions ($\mathbf{u}_\perp$ is continuous and u_z is exactly zero at the interfaces, where $\mathbf{u}$ is the phonon displacement). A more detailed analysis of the electron–optical-vibration interaction is given elsewhere.[14]

It is clear from Eq. (7) that in order to evaluate the Raman polarizability, it is necessary to know the excitonic states Ψ_μ and the matrix elements $\langle \Psi_{\mu_2} | \Phi_F^{(n)}(z_e)e^{-i\mathbf{q}\cdot\mathbf{r}_e} | \Psi_{\mu_1} \rangle$ in the quantum disk. In the following we consider the excitonic

effects in the framework of the Wannier model for the electron-hole pairs confined to semiconductor SAQDs with elliptical cross section.

A. Excitonic states

The excitonic wave functions are taken as a solution of the Hamiltonian

$$H = H_e + H_h - \frac{e^2}{\varepsilon\sqrt{(x_e - x_h)^2 + (y_e - y_h)^2 + (z_e - z_h)^2}}, \quad (11)$$

where

$$H_i(\mathbf{r}_i) = p_{iz}\left(\frac{1}{2m_z^i(z_i)}\right)p_{iz} + \frac{1}{2m_\perp^i}p_{i\perp}^2 + \frac{1}{2}m_\perp^i(\omega_x^2 x_i^2 + \omega_y^2 y_i^2)$$
$$+ V(z_i). \quad (12)$$

Here, $m_\perp^i$ ($\mathbf{p}_{i\perp}$) and m_z^i (p_{iz}) ($i = e,h$) are the carrier effective masses (momentum operators) in the XY plane and the Z axis, respectively, $V(z_i)$ is the carrier confinement potential, and ε is the dielectric constant (notice we ignore small image charge effects here, although they could be introduced straightforwardly). For flat quantum disks, where the condition $L_x, L_y \gg L_z$ is fulfilled, the anisotropic effect along the Z axis can be disregarded. The effective mass $m_z^i(z_i)$ and carrier confinement potential are taken as steplike functions. That is, the potential $V(z_i)$ and $m_z^i(z_i)$ have constant values in and outside the QD. On the other hand, the shape and confinement anisotropies in the XY plane are modeled by harmonic potentials with frequencies ω_x and ω_y, where $\sqrt{\omega_y/\omega_x} = L_x/L_y$.[15] In this case, where $L_x, L_y \gg L_z$, the lateral confinement is weaker than along the perpendicular direction. Therefore, the excitonic Bohr radius a_B is much larger than the electron-hole pair mean value along the Z direction, and the excitonic motion can be considered decoupled from the Z component. Hence, Eq. (11) can be cast as

$$H(\mathbf{r}_e, \mathbf{r}_h) = H_0(\mathbf{r}_e, \mathbf{r}_h) + H_p(\mathbf{r}_e, \mathbf{r}_h), \quad (13)$$

$$H_0(\mathbf{r}_e, \mathbf{r}_h) = H_e(\mathbf{r}_e) + H_h(\mathbf{r}_h) - \frac{e^2}{\varepsilon|\boldsymbol{\rho}_e - \boldsymbol{\rho}_h|}, \quad (14)$$

and H_p is a perturbation term given by

$$H_p(\mathbf{r}_e, \mathbf{r}_h) = -\frac{e^2}{\varepsilon}\{[(\boldsymbol{\rho}_e - \boldsymbol{\rho}_h)^2 + (z_e - z_h)^2]^{-1/2}$$
$$- |\boldsymbol{\rho}_e - \boldsymbol{\rho}_h|^{-1}\}, \quad (15)$$

where $\boldsymbol{\rho}$ is the carrier coordinate in the XY plane. The solution of the Hamiltonian H_0 is readily written in separable form by a product of the wave function in the plane and the electron and hole subband wave functions $\phi_i(z_i)$. The exciton in-plane motion is described using the center-of-mass coordinates $\mathbf{R} = (m^e\boldsymbol{\rho}_e + m_\perp^h\boldsymbol{\rho}_h)/(m^e + m_\perp^h) = X\hat{x} + Y\hat{y}$, and $\boldsymbol{\rho} = \boldsymbol{\rho}_e - \boldsymbol{\rho}_h = x\hat{x} + y\hat{y}$. Correspondingly, the exciton envelope function can be written as
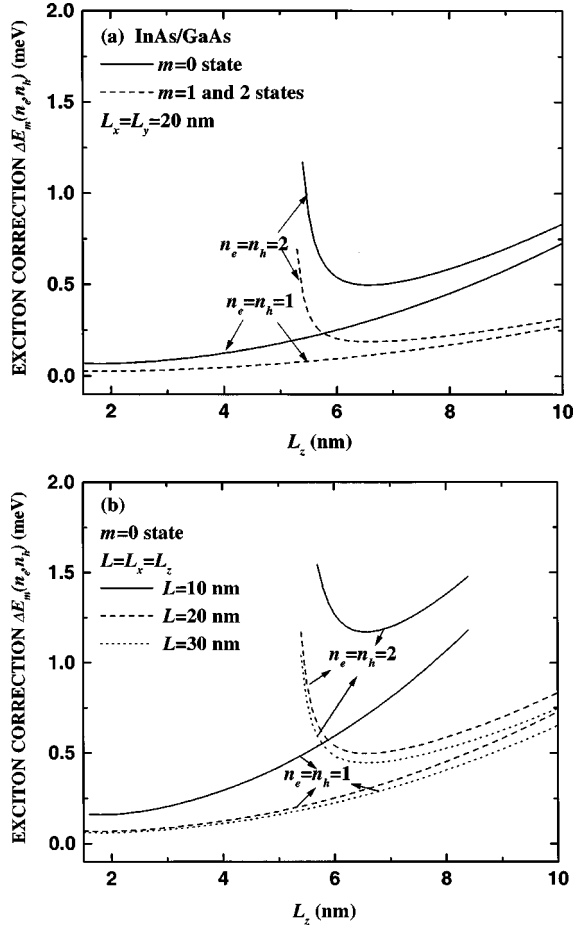
FIG. 2. Three-dimensional Coulomb potential correction $\Delta E_m(n_e, n_h)$ in an InAs/GaAs SAQD with circular cross section, as a function of the quantum dot size L_z. The first two electron and hole subbands n_e, $n_h = 1,2$ are considered. (a) $L = \sqrt{L_x L_y} = 20$ nm, and in-plane internal exciton quantum number $m=0$ (solid lines), and degenerate $m=1$ and 2 (dashed). (b) $\Delta E_0(n_e, n_h)$ for $L=10$ nm (solid lines), $L=20$ nm (dashed), and $L=30$ nm (dotted).

$$\Psi_\mu(\mathbf{r}_e, \mathbf{r}_h) = \phi_{n_e}(z_e) \phi_{n_h}(z_h) \varphi_{N_x, N_y}(\mathbf{R}) \Theta_m(\boldsymbol{\rho}). \quad (16)$$

The functions $\phi_{n_e}(z_e)$ [$\phi_{n_h}(z_h)$], $\varphi_{N_x,N_y}(\mathbf{R})$, and $\Theta_m(\boldsymbol{\rho})$ represent the confinement of the carrier by the $V(z_e)$ [$V(z_h)$] band profile in the n_eth [n_hth] Z-level, the two-dimensional (2D) center-of-mass motion of the exciton with quantum number N_x and N_y, and the relative in-plane exciton motion in the mth state, respectively. The solutions for these functions as well as the contribution to the total exciton energy given by the perturbation Hamiltonian H_p are discussed in the Appendix. The purely 2D exciton problem described by H_0 in Eq. (14) has been solved by direct matrix diagonalization in a basis of optimized harmonic oscillators, as described in Ref. 15. We refer the reader to that work for details of the resulting excitonic states in 2D. In the current work, moreover, we include the 3D character of the problem via the $\phi(z)$ functions and the correction provided by H_p in Eq. (15).

Figure 2 presents the numerical results for the three-dimensional exciton correction $\langle \Psi_\mu | H_p | \Psi_\mu \rangle = \Delta E_m(n_e, n_h)$

TABLE I. Parameters used in calculations. If heavy- and light-hole [(hh) and (lh)] masses do not appear explicitly in the reference cited, they were calculated from the bulk Luttinger parameters γ_1 and γ_2, as described in text.

Parameters	InAs	GaAs	CdSe	ZnSe
E_g (eV)	0.45[a]	1.51[a]	1.84[a]	2.82[a]
ε_0	14.6[a]		9.3[e]	
ω_L (cm^{-1})	259.7[b]	292[a]	209[a]	250[a]
β_L	1.389×10^{-6} [c]		1.576×10^{-6} [d]	
m^e/m_0	0.023[a] 0.08[f]	0.067[a]	0.112[e]	0.16[a]
m_z^h/m_0	0.34 (hh)[a] 0.027 (lh)[a] 0.08[e]	0.38 (hh)[a] 0.09 (lh)[a]	1.2[f]	0.38[a]
$m_\perp^h/m_0$	0.036 (hh)[a] 0.088 (lh)[a] 0.08[e]		0.45[e]	
ΔE_c (%)	40%		40%	
ΔE_v (%)	60%		60%	
Γ_p (cm^{-1})	2		2	

[a]Reference 23.
[b]Reference 5.
[c]Reference 20.
[d]Reference 24.
[e]Reference 25.
[f]Reference 26.

in InAs/GaAs quantum disks. We have used the values given in Table I for the calculations, with $m^e = 0.023m_0$, $m_z^h = 0.34m_0$, and $m_\perp^h = 0.036m_0$. The ΔE_m contribution to the exciton energy for circular cross section with $L_x = L_y = 20$ nm is shown in Fig. 2(a) as a function of the quantum dot size L_z ranging from 2 to 10 nm. Different internal quantum numbers $m=0$ (solid lines) and $m=1$ and 2 (dashed lines) are shown for the first two electron and hole subbands $n_e = n_h = 1$ and 2. As L_z decreases, the exciton becomes more two dimensional and the 3D energy correction is expected to decrease, as seen in general. At a certain value $(L_z = L_{z0})$, however, ΔE_m reaches a minimum and for $L_z < L_{z0}$ it grows rapidly. For smaller L_z values the quantum confined carrier energy is close to the band offset energy and the carrier wave function penetrates into the surrounding medium. That is, the carrier becoming less confined. The minimum position L_{z0} strongly depends on the electron and hole subbands, as seen in Fig. 2(a). We have limited the curves in Fig. 2 for values of L_z satisfying the condition $\langle n_e, n_h | z_e^2 + z_h^2 | n_e, n_h \rangle = 0.25 r_s^2(m)$, which corresponds to $L_z \sim 5$ nm for the exciton branch $n_e = n_h = 2$. As the perturbation ΔE_m has been calculated under the approximation $\langle n_e, n_h | z_e^2 + z_h^2 | n_e, n_h \rangle < r_s^2(m)$ (see Appendix), it is no longer valid for smaller values of L_z. In the regime where L_z is very small, the exciton returns to a 3D character, although with a "pinned"

center of mass. In fact, the confinement is so strong that the electron is found with large probability outside the QD, while being bound to the hole (which is trapped inside the disk due to its heavier mass $m_z^h \gg m^e$) by the Coulomb interaction.

Figure 2(b) is devoted to the variation of ΔE_0 for values of $L = L_x = L_y$ ranging from 10 to 30 nm. As the disk radius gets larger, in-plane internal motion is less confined and $\Delta E_m(n_e, n_h)$ tends to a fixed value nearly independent of L and subband quantum numbers n_e, n_h. In the case of Fig. 2(b), that takes place for $L \gtrsim 30$ nm. Similar results to those presented in Fig. 2 were obtained for a SAQD with elliptical cross section (not shown). Using this correction for the general case, the total exciton energy is equal to

$$E(m, N_x, N_y, n_e, n_h) = E_g + (N_x + 1/2)\hbar\omega_x + (N_y + 1/2)\hbar\omega_y$$
$$+ E_{n_e} + E_{n_h} + E_m + \Delta E_m(n_e, n_h), \tag{17}$$

where E_g is the gap energy. As we have seen, for all cases studied under the conditions $L_z \ll L_x, L_y$, the contribution of ΔE_m to the exciton binding energy is very small and, in first approximation, it could be disregarded. We include it in our numerical results for completeness.

B. Matrix elements

Following the results of the Appendix for the exciton wave function, the corresponding coefficient T_{cv}^μ can be written as

$$T_{cv}^\mu = 2\frac{e}{m_0}\mathbf{e}\cdot\mathbf{p}_{cv}\left(\frac{2\pi\hbar}{V\omega\eta^2}\frac{\mu}{M}\frac{N_x!N_y!}{2^{N_x+N_y}\left[\left(\frac{N_x}{2}\right)!\left(\frac{N_x}{2}\right)!\right]^2}\right)^{1/2}\sum_{n_x,n_y}A(n_x)A(n_y)a_{2n_x,2n_y}(m)\int_{-\infty}^{\infty}\varphi_{n_e}(z)\varphi_{n_h}(z)dz, \tag{18}$$

with $A(n) = (-1)^n(2n-1)!!/\sqrt{(2n)!}$. The direct allowed optical transitions are those that produce excitons in the mth excitonic state for $n_e - n_h$ equal to an even number (for a symmetric well), while the center-of-mass quantum numbers N_x, N_y in the XY plane must also be even. Therefore, we only need to evaluate the $a_{2n_x,2n_y}$ coefficients for each exciton state m [with a_{n_x,n_y} defined as per Eq. (A9)].

For the exciton-phonon matrix interaction proportional to $\langle\Psi_{\mu'}|\Phi_F^{(n)}(z)e^{-i\mathbf{q}\cdot\mathbf{r}}|\Psi_\mu\rangle$, and involved in Eq. (7), we find that (for μ: $\{n_e, n_h, N_x, N_y, m\}$),

$$\langle m', N_x', N_y'; n_e', n_h'|\Phi_F^{(n)}(z_e)e^{-i\mathbf{q}\cdot\mathbf{r}_e}|n_e, n_h; N_y, N_x, m\rangle = \langle m'|e^{-i\mathbf{q}\cdot\boldsymbol{\rho}m_h/M}|m\rangle\langle n_e'|\Phi_F^{(n)}(z_e)|n_e\rangle\delta_{n_h',n_h}\langle N_x'|e^{-iq_xX}|N_x\rangle$$
$$\times\langle N_y'|e^{-iq_yY}|N_y\rangle, \tag{19}$$

where the separability of the wave functions Ψ_μ has been used, and

$$\langle N'|e^{-iq_xX}|N\rangle = \exp\left(-\frac{q_x^2}{4\alpha_M^2}\right)\min\left[\sqrt{\frac{N'!}{N!}}, \sqrt{\frac{N!}{N'!}}\right]^2\left(-\frac{iq_x}{\sqrt{2}\alpha_M}\right)^{|N'-N|}L_{\max(N,N')}^{|N'-N|}\left[\left(\frac{q_x}{\sqrt{2}\alpha_M}\right)^2\right], \tag{20}$$

with $\alpha_M^2 = M\omega_x/\hbar$, M is the total exciton mass, and $L_a^b(\xi)$ are the associated Laguerre polynomials. From the above equation it is clear that for larger L_x in comparison with the lattice constant a_0, the main contribution to Eq. (20) comes from $q_x = 0$. In this case, it is possible to show that Eq. (20) reduces to $\delta_{N',N}$. Thus, the exciton-phonon matrix elements are given by

$$\langle\Psi_{\mu'}|\Phi_F^{(n)}(z_e)e^{-i\mathbf{q}\cdot\mathbf{r}_e}|\Psi_\mu\rangle = \delta_{N_x',N_x}\delta_{N_y',N_y}\delta_{m',m}\delta_{n_h',n_h}\langle n_e'|\Phi_F^{(n)}(z_e)|n_e\rangle. \tag{21}$$

A similar expression is obtained for the contribution from holes. The matrix elements of the Fröhlich potential $\Phi_F^{(n)}(z)$ between n_i' and n_i electronic states are straightforward calculations and will not be presented here. The most important case $n_i = n_i'$ can be cast as

$$\langle n_i|\Phi_F^{(n)}(z)|n_i\rangle = (-1)^{n+1}\left\{\frac{1}{k_B} + \frac{1}{k_A}\frac{m_Ak_B}{m_Bk_A} + \frac{L_z}{2}\left[1 + \left(\frac{m_Ak_B}{m_Bk_A}\right)^2\right]\right\}^{-1}\left\{\frac{1}{k_A}\frac{m_Ak_B}{m_Bk_A}\frac{1}{1-(2k_AL_z/n\pi)^2} + \frac{L_z}{2}\left[1 + \left(\frac{m_Ak_B}{m_Bk_A}\right)^2\right]\right\}. \tag{22}$$

It is important to emphasize that in the dipole approximation ($q = 0$) the Fröhlich mechanism for Raman scattering is not allowed in bulk semiconductors.[16] This rule is broken due to the different confinement of electron and hole, which results in a noncancellation effect of the matrix element (for $q = 0$), whenever a nanostructure is considered. This difference between electrons and holes is known as ''decompensation.''[8] In nanostructures, this effect arises due to the finite potential barrier and their different masses, and/or due to electron-hole correlation. The values of the Raman scattering cross section in the $Z(X,X)\bar{Z}$ configuration depend on the differences between electron and hole wave

functions through the Fröhlich Hamiltonian. In our approach, if an infinite barrier along the growth direction is assumed, the Fröhlich contribution to the Raman scattering vanishes, since in that case, the mass asymmetry does not play a role in determining the wave functions.

For the Z-confinement model assumed, symmetric along that axis, Eq. (21) restricts the phonon modes to only even values, $n=2,4,\ldots$, and no odd numbers contribute to the cross section. Hence, the following selection rules are obtained for the quantum numbers involved in Eqs. (7) and (18):

$$|n_e-n_h|=0,2,\ldots; \quad N_x,N_y=0,2,4,\ldots, \quad \text{with}$$

$$\Delta N_{x,y}=0; \quad m=0,1,\ldots; \quad n=2,4,\ldots. \quad (23)$$

That these selection rules are obeyed will allow us to clearly identify the various contributions to the Raman scattering cross section and intensity, as we will see in the next section.

III. RAMAN POLARIZABILITY

The diagonal component of the Raman tensor a_F for the nth phonon can be obtained by introducing the calculated matrix elements into Eq. (2), so that

$$a_F^{(n)}=-ia_{0F}\sum_{N_x,N_y}\frac{N_x!N_y!}{2^{N_x+N_y}\left[\left(\frac{N_x}{2}\right)!\left(\frac{N_y}{2}\right)!\right]^2}$$

$$\times\sum_m \Theta_m^2(0) \sum_{n_e,n_h,n_e',n_h'} \int_{-\infty}^{\infty}\phi_{n_e'}^*\phi_{n_h'}^*dz$$

$$\times\frac{1}{[\hbar\omega_l-E(m,N_x,N_y;n_e,n_h)+i\Gamma_1]}\int_{-\infty}^{\infty}\phi_{n_e}\phi_{n_h}dz$$

$$\times\frac{1}{n}\left[\frac{\delta_{n_h',n_h}\langle n_e'|\Phi_F^{(n)}|n_e\rangle}{[\hbar\omega_s-E(m,N_x,N_y;n_e',n_h)+i\Gamma_2]}\right.$$

$$\left.-\frac{\delta_{n_e',n_e}\langle n_h'|\Phi_F^{(n)}|n_h\rangle}{[\hbar\omega_s-E(m,N_x,N_y;n_e,n_h')+i\Gamma_2]}\right], \quad (24)$$

where

$$a_{0F}=4\frac{e^3}{m_0^2}\sqrt{\frac{\pi a_0^3M^*}{\omega_l\omega_s}}\frac{\mu^2}{M}\frac{\sqrt{\omega_x\omega_y}}{\hbar\omega_l}\sqrt{\frac{(\omega_L^2-\omega_T^2)}{\varepsilon_\infty}}\frac{fP^2}{\pi}, \quad (25)$$

M^* is the reduced mass of the *atoms* involved in the optical mode, $P=|\langle x|p_x|s\rangle|$, f is equal to 1 or 1/3 for the heavy- or light-hole contribution, respectively, and the approximation $\omega_L\approx\omega_n$ has been used to obtain Eq. (25).

The Raman polarizability, the Raman scattering efficiency per unit length and unit solid angle for a given final confined phonon, $\partial S^{(n)}/\partial\Omega$ (also known as Raman intensity), and the differential Raman cross section $\partial^2\sigma/\partial\Omega\partial\omega_s$ per unit of solid angle are given by the equations

$$\frac{\partial S^{(n)}}{\partial\Omega}=V\frac{\eta_s}{\eta_l}\frac{\omega_s^3\omega_l}{c^4}\left(\frac{u_0}{V_c}\right)^2|a_F^{(n)}|^2 \quad (26)$$

and

$$\frac{\partial^2\sigma}{\partial\Omega\partial\omega_s}=V^2\frac{\eta_s}{\eta_l}\frac{\omega_s^3\omega_l}{c^4}\left(\frac{u_0}{V_c}\right)^2\sum_n |a_F^{(n)}|^2\delta(\omega_s-\omega_l-\omega_n). \quad (27)$$

The Bose-Einstein phonon factors in Eqs. (26) and (27) are neglected because we consider Raman processes at low temperature, so that the number of thermal phonons is negligible. The two denominators in Eq. (24) can produce resonances at different photon energies. The first one (*incoming resonance*) at $\hbar\omega_l=E(m,N_x,N_y;n_e,n_h)$, and the second one (*outgoing resonance*) at $\hbar\omega_s=E(m,N_x,N_y;n_e,n_h')$ or $\hbar\omega_s=E(m,N_x,N_y;n_e',n_h)$ which correspond to phonon emission by electrons or holes, respectively. As in photoluminescence excitation measurements, the Raman scattering efficiency profile (for a given pair n_e,n_h of electron and hole subbands) describes excitonic states with even center-of-mass quantum numbers and oscillator strength equal to $\Theta_m^2(0)$.[15] Quantum disks with circular cross section present a degeneracy of order $N+1$, where $N=N_x+N_y$, due to their XY symmetry. Therefore, the excitonic states satisfying the condition $N_x+N_y=N$, with N_x,N_y being even numbers, contribute to the same peak in the Raman profile. On the other hand, for elliptical cross section ($L_x\neq L_y$), the center-of-mass and relative motion degeneracies are broken, and due to the reduction in the density of states, the observed Raman peaks will be smaller than those observed in the circular cross-section case. The relative energy position of the peaks in the Raman scattering efficiency profiles and their amplitudes give a direct measurement of the ratio L_x/L_y and the quantum disk geometry.

In the following, we analyze the Raman processes for the case of InAs/GaAs and CdSe/ZnSe SAQD's. The incoming (outgoing) resonances are denoted by the symbol I (O) in the figures, and the main excitonic state contributions by the set of quantum numbers (m,N_x,N_y). For simplicity, and to illustrate the effectiveness of this technique, we have only considered an incoming frequency range belonging to the excitonic branch $n_e=n_h=1$, with the material parameters listed on Table I. Considering incoming resonance with other excitonic branches would give rise to contrasting information related to differences in excitonic wave functions and matrix elements. A full analysis of the Raman response in each system should provide vast supplementary information to PLE and PL spectra to characterize completely the SAQDs involved, and the confinement potentials that give rise to these exciton states.

A. InAs/GaAs

Figure 3 displays the Raman intensity profiles for the $n=2$ LO confined mode of InAs dots embedded in a GaAs matrix, in the vicinity of the fundamental absorption edge, for the cases of (a) circular geometry, (b) elliptical cross section (with $L_y=2L_x$). Vertical lines (terminated by a filled circle for I resonances and by a dark square for O resonances) represent the strength of the main contribution to each resonant peak. It should be noticed that for closely spaced peaks the interference between different resonant levels is strong and the total intensity is not simply the result of
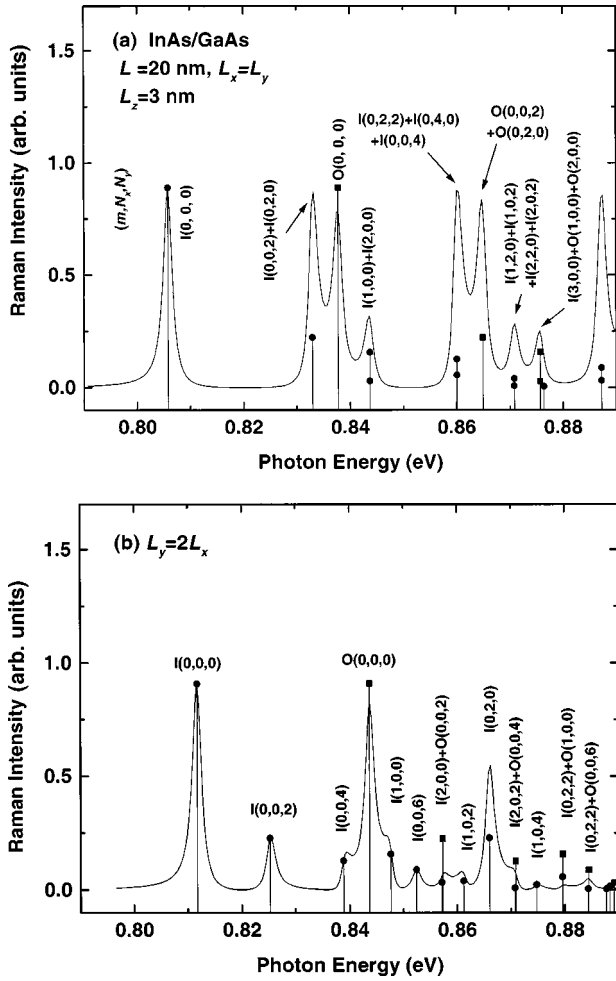
FIG. 3. Raman intensity as per Eq. (26) as a function of laser energy for InAs dots in GaAs. Figures correspond to the $n=2$ LO confined mode of InAs with $m^e=0.023m_0$, $m_z^h=0.34m_0$, and $m_\perp^h=0.036m_0$. (a) Circularly symmetric case with $L_z=2$ nm, and $L_x=L_y=20$ nm. (b) Asymmetric QD with $L_z=2$ nm, $L=\sqrt{L_xL_y}=20$ nm, and $2L_x=L_y$. The incoming (I) and outgoing (O) resonances are labeled by their quantum numbers (m,N_x,N_y), with $n_e=n_h=1$ in all cases. The strength of the main contribution to the incoming (outgoing) resonance is indicated by a vertical line with a filled circle (square).

single contributions. This effect is strongest in the case of circular geometry, shown in Fig. 3(a). The Raman profile displays a series of center-of-mass peaks for each exciton internal state m, closely resembling the excitonic oscillator strength. For the case of circular geometry, the states with $N_x+N_y=N$ are all degenerate and the Raman features appear then as relatively large resonant peaks for laser energy equal to the incoming or outgoing energy transitions. Note, in fact, that there are many doubly annotated features in Fig. 3(a), such as (0,0,2) and (0,2,0), indicating degeneracies. In contrast, Fig. 3(b) clearly shows that we are dealing with elliptical cross-section dots, since the circular symmetry degeneracy is lifted, and a diverse set of incoming and outgoing resonances appear in the Raman scattering efficiency. The relatively small peaks, rare interference, and overall frequency splitting between peaks are a direct indication of the QD anisotropy. Note, in particular, that the transitions involving the ground state (0,0,0) are substantially stronger,
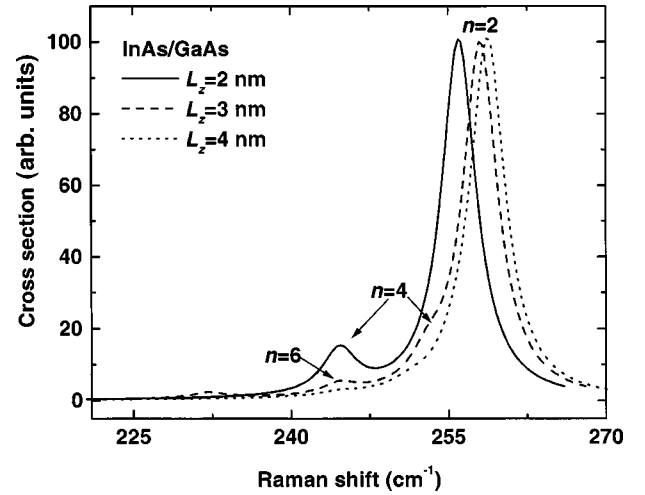
FIG. 4. Raman cross section of InAs/GaAs SAQDs with circular symmetry, $L=\sqrt{L_xL_y}=20$ nm, and L_z varying from 2 to 4 nm, at $\hbar\omega_l$ in *incoming* resonance with the lowest exciton level. Contribution of different phonon modes n as indicated.

both in the I and O channels. Similarly, the large gap (~ 30 meV) between the first two peaks in Fig. 3(a) is now much smaller (~ 15 meV) in Fig. 3(b), due to the lower symmetry of this dot.

Let us now look at the overall Raman cross section in this system. Figure 4 shows this quantity for the SAQDs of lateral dimension $L=4$ nm and three different values of thickness $L_z=2$, 3, and 4 nm, at $\hbar\omega_l$ in the incoming resonance with the lowest excitonic state ($m=N_x=N_y=0$, $n_e=n_h=1$). The InAs bulk phonon frequency of 259.7 cm^{-1} used to evaluate the InAs/GaAs SAQD phonon dispersion takes into account the lattice mismatch stress and the growth conditions.[5] The δ function in Eq. (27) has been replaced by a Lorentzian with phonon linewidth $\Gamma_p=2$ cm^{-1}. The phonon frequency depends on L_z due to the phonon confinement as given by Eq. (9). The calculated Raman spectra show similar behavior in the case of circular geometry ($L_x=L_y$) or elliptical cross section (with $L_y=2L_x$). It can be seen in Fig. 4 that the $n=4$ phonon peak increases as L_z decreases (apart from a shift in energy). This can be explained through the denominator $[1-(2k_AL_z/n\pi)^2]$ in Eq. (22). This factor has a minimum for $n=2$ as $k_AL_z\lesssim\pi$ (the equality is achieved in the limit of an infinitely deep well or large L_z values). This fact explains why the relative intensity $I_{n=2}/I_{n=4}$ decreases as L_z decreases. It can be noted that for $L_z\lesssim 5$ nm we have only one exciton branch ($n_e=n_h=1$) contributing to the cross section.

Role of carrier masses

Let us comment on the important effects of the various components of the carrier effective masses on the Raman profile. First, we observe that the confinement induced renormalization of the fundamental edge is a sensitive function of the carrier masses along the growth direction and the band offsets. Second, the shape of the Raman profiles is determined to a great extent by the in-plane motion, and consequently, by the carrier in-plane masses. Thirdly, the absolute values of the Raman intensity strongly depend on the electron-hole decompensation effect in the growth direction,[8]
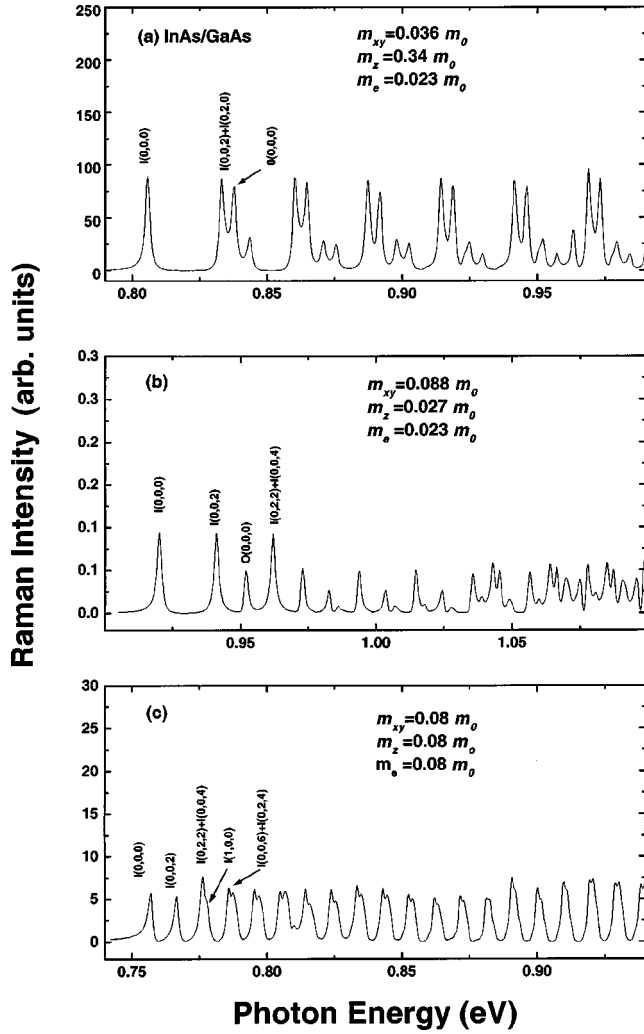
FIG. 5. Raman intensity profiles calculated for different sets of hole mass values, for InAs quantum disks in GaAs, with $L_z = 2$ nm and $L_x = L_y = 20$ nm. Masses as indicated in each panel: (a) $m^e = 0.023m_0$, $m_z^h = 0.34m_0$, $m_\perp^h = 0.036m_0$, as in Fig. 3(a); (b) $m^e = 0.023m_0$, $m_z^h = 0.027m_0$, $m_\perp^h = 0.088m_0$; (c) $m^e = 0.08m_0$, $m_z^h = 0.08m_0$, $m_\perp^h = 0.08m_0$. Incoming (I) and outgoing (O) resonances indicated as in Fig. 3.

which, as discussed above, depends on the Z masses and band offsets. Figure 5 shows the Raman intensities (for the $n = 2$ LO phonon) calculated using different sets of masses (see Table I): (a) bulk m_z heavy hole ($m_\perp$ exhibits a light-hole character), (b) bulk m_z light hole ($m_\perp$ is now the heavier one), and (c) isotropic masses $m^e = m^h = 0.08m_0$. The light-hole contribution to the scattering efficiency is about 900 times weaker than that corresponding to the heavy hole, due to the factor $f = 1/3$ in Eq. (25) and that the electron and light-hole masses in the bulk are very close ($m^e = 0.023m_0$, and $m_z^h = 0.027m_0$). The effective hole masses used in the calculation of Figs. 5(a) and 5(b) arise from the diagonal components of the 4×4 $\mathbf{k} \cdot \mathbf{p}$ Hamiltonian.[17] The masses are derived from the bulk Luttinger parameters γ_1 and γ_2, where $m_z^h = m_0/(\gamma_1 \mp 2\gamma_2)$ and $m_\perp^h = m_0/(\gamma_1 \pm \gamma_2)$. The case of Fig. 5(c) is intermediate between (a) and (b), and is presented only to illustrate how different masses affect the Raman intensity profiles. In this last case, decompensation differences between the hole and electron wave functions are due only to
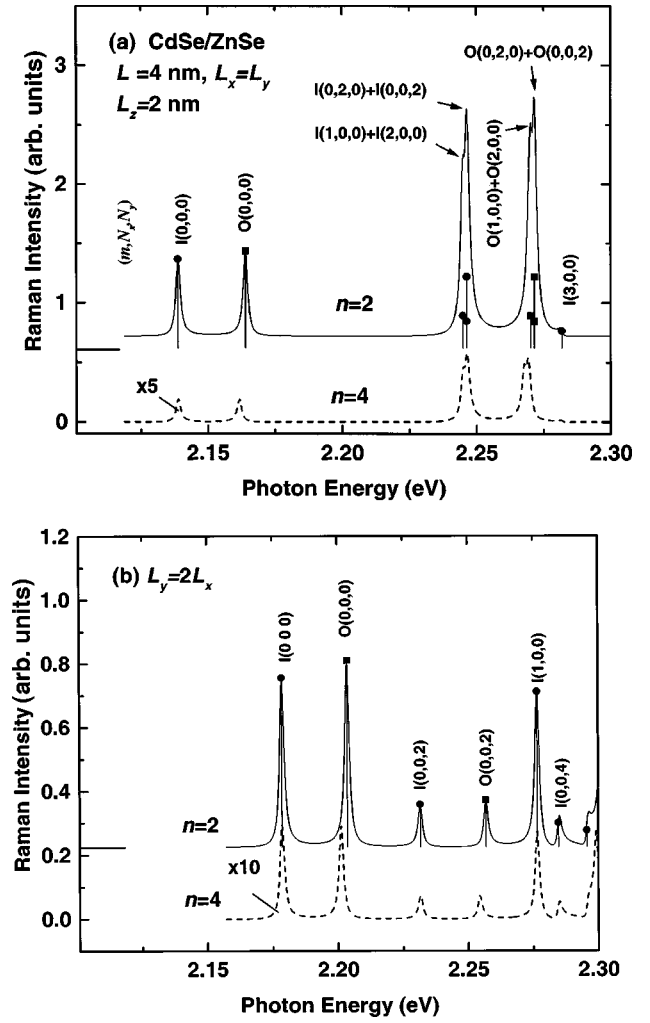
FIG. 6. Raman scattering efficiency as a function of $\hbar\omega_l$ for CdSe/ZnSe SAQDs for the $n = 2$ and $n = 4$ LO confined modes of CdSe. (a) Circular cross section, where $L_x = L_y = 4$ nm and $L_z = 2$ nm. (b) Elliptical cross section with $L = \sqrt{L_x L_y} = 4$ nm, $L_y = 2L_x$, and $L_z = 2$ nm. Notation as in Fig. 3. Notice much weaker contribution from $n = 4$ modes.

the different conduction- and valence-band offsets. Notice, by comparing all three panels, that the more symmetric $m_\perp$ and m_e are, the more periodic the various excitonic levels appear in the Raman profiles. As mentioned before, given that the carrier masses affect the Raman response so strongly, one could, in principle, use the experimental results in a given system to extract information on the masses. This would be a very specific and powerful technique to provide carrier masses in the relatively complex environment of the SAQDs, where strains, facetting, and even hole mixing makes their theoretical prediction and estimation quite difficult.

B. CdSe/ZnSe

To illustrate the role of the specific materials that compose the SAQD, Fig. 6 shows the Raman scattering efficiency as a function of the laser energy for CdSe dots in a ZnSe substrate. Typically, the CdSe/ZnSe quantum disk islands are obtained by atomic layer epitaxy or by molecular-beam epitaxy.[18,19] Here, as before, we show the case of the

$n=2$ LO confined phonon for a quantum disk with circular cross section in (a), and for a nonsymmetric one in (b). In Fig. 6(a) $L_x=L_y=4$ nm and $L_z=2$ nm, while in Fig. 6(b) $L=\sqrt{L_xL_y}=4$ nm, but $L_y=2L_x$ and $L_z=2$ nm. As in Fig. 3, the vertical lines represent the relative strength of the main excitonic transitions in the total Raman intensity, all of them corresponding to the exciton branch with $n_e=n_h=1$. The set of parameters used is given in Table I. To obtain the phonon dispersion we used the bulk frequency of $\omega_L=209$ cm^{-1} and $\omega_L=250$ cm^{-1} for CdSe and ZnSe, respectively, following the confined phonon model described in Sec. II. Here, the lattice mismatch stress and the growth conditions have not been taken into account, mainly due to the lack of knowledge concerning the phonon frequencies on this type of SAQD's. An estimation using pseudomorphic strains would shift the CdSe frequency to $\omega_L\approx239$ cm^{-1},[20] for which there is recent experimental evidence,[21] although further verification is needed.

The principal features of the resonance profile present in Fig. 6 are as follows: First, the outgoing resonances are slightly higher than the incoming ones. Second, additional peaks appear in between $I(0,N_x,N_y)$ and $I(1,N_x,N_y)$ when the circular symmetry is broken, just as in the InAs case, with the number of visible peaks increasing with the quantum disk lateral dimensions. Here, we also show the corresponding contribution from the $n=4$ phonon mode. As before, this results in a much weaker peak, although the small energy shift is clearly visible and likely measurable in cross-section plots. In comparison with Fig. 3, note how successive I or O peaks appear much farther here, as the lateral size is smaller in this case, producing stronger quantization despite a larger $m_\perp^h$ mass. In fact, as the exciton size (or effective Bohr radius) is quite small in this material, $L\gtrsim10$ nm would yield very weak quantum confinement and a more continuum density of states.

IV. CONCLUSIONS

We have presented a theoretical formulation for the one-phonon resonant Raman profile and cross section in SAQD's with flat cylindrical symmetry. We find that the pattern of the scattered light intensity is characterized by the hole in-plane mass and lateral confinement anisotropies, while effective masses and disk thickness along the growth direction determine to a great extent the Raman spectra and their absolute values. The Raman selection rules obtained for the in-plane center-of-mass quantum numbers $\Delta N_x=\Delta N_y=0$, allow a qualitative evaluation of the anisotropy geometry of the island. The difference in frequency between any two incoming (or outgoing) resonance peaks in the Raman scattering efficiency profile is proportional to the square lateral confinement $[(N_x-N_x')L_x^{-2}+(N_y-N_y')L_y^{-2}]$. We also find that the Raman spectra are nearly independent of the ratio L_x/L_y, even when the intensity depends strongly on that ratio.

We have also shown how the relative values of the various carrier masses change the Raman response in a qualitative fashion. This sensitivity to the masses can, in turn, be used to characterize the system not only as far as phonon dispersions (which control to a great extent the *position* of the Raman features), but also the effective masses of holes and electrons participating in the scattering (which change

substantially the relative intensities and various peak splittings).

One should comment, moreover, that perhaps the most natural and unambiguous comparison of our calculations with experiments would occur for results of micro-Raman probes. Current probes sample typically the entire dot ensemble in the system and yield naturally a convolution of the single dot response with the distribution. Sample or strain field inhomogeneities would make the analysis more involved and likely not as precise. The local probe, on the other hand, is a fascinating technique capable of not only studying the frequency dependence of the Raman yield (exploring both incoming and outgoing resonances), but it also gives information on the *spatial* dependence of the cross sections.[21]

APPENDIX

1. The Z motion of the carrier

In the effective-mass approximation the Z motion of the carriers is described by the Schrödinger equation

$$\left[p_z\left(\frac{1}{2m(z)}p_z\right)+V(z)\right]\phi_n(z)=E_n\phi_n(z), \quad \text{(A1)}$$

and

$$V(z)=\begin{cases} 0; & |z|\leq\dfrac{L_z}{2} \\ V_0; & |z|\geq\dfrac{L_z}{2} \end{cases}; \quad m(z)=\begin{cases} m_A; & |z|\leq\dfrac{L_z}{2} \\ m_B; & |z|\geq\dfrac{L_z}{2}. \end{cases} \quad \text{(A2)}$$

The bound states are therefore given by

$$\phi_n(z)=\left[\frac{1}{k_B}+\frac{1}{k_A}\frac{m_A}{m_B}\frac{k_B}{k_A}+\frac{L_z}{2}\left(\frac{m_A}{m_B}\frac{k_B}{k_A}\right)^2+\frac{L_z}{2}\right]^{-1/2}$$
$$\times\begin{cases} e^{k_B(z-L_z/2)}; & z\leq-\dfrac{L_z}{2} \\ \dfrac{\cos[k_Az+(n-1)\pi/2]}{\cos[k_AL_z/2+(n-1)\pi/2]}; & |z|\leq\dfrac{L_z}{2} \\ (-1)^{n+1}e^{-k_B(z-L_z/2)}; & z\geq-\dfrac{L_z}{2}, \end{cases}$$

$$\text{(A3)}$$

with $n=1,3,\dots$ for even parity states and $n=2,4,\dots$ for odd parity states, $k_A=\sqrt{2m_AE_n/\hbar^2}$, $k_B=\sqrt{2m_B(V_0-E_n)/\hbar^2}$, and m_A (m_B) is the effective mass in the well (barrier). The bound state conditions result in the following transcendental equations:

$$\frac{k_B}{m_B}=\frac{k_A}{m_A}\begin{cases}\tan\left(\dfrac{k_A L_z}{2}\right); & n=1,3,\ldots \\[2mm] -\cot\left(\dfrac{k_A L_z}{2}\right); & n=2,4,\ldots \end{cases} \qquad (A4)$$

2. Two-dimensional exciton center-of-mass motion

The wave function of the exciton center-of-mass motion $\varphi_{N_x,N_y}(\mathbf{R})$ corresponds to a two-dimensional harmonic oscillator in the XY plane with quantum numbers N_x,N_y given by[15]

$$\varphi_{N_x,N_y}(\mathbf{R})=\varphi_{N_x}(x)\varphi_{N_y}(y), \qquad (A5)$$

where

$$\varphi_N(x)=\left(\frac{\alpha_M}{\sqrt{\pi}2^N N!}\right)^{1/2}\exp(-\alpha_M^2 x^2/2) \quad H_N(x), \quad (A6)$$

$\alpha_M=\sqrt{M\omega_x/\hbar}$, $M=m_{xy}^e+m_{xy}^h$, the function $H_N(x)$ is the Hermite polynomial,[22] and the center-of-mass energy is given by

$$E_{cm}=\left(N_x+\frac{1}{2}\right)\hbar\omega_x+\left(N_y+\frac{1}{2}\right)\hbar\omega_y. \qquad (A7)$$

3. Exciton relative motion

The Hamiltonian describing the relative motion of the 2D exciton is given by[15]

$$H_{rel}=\frac{p^2}{2\mu}+\frac{1}{2}\mu\omega_x^2 x^2+\frac{1}{2}\mu\omega_y^2 y^2-\frac{e^2}{\varepsilon\sqrt{x^2+y^2}}, \quad (A8)$$

where μ is the exciton reduced mass in the XY plane. The 2D exciton is confined along the X and Y axes by the har-

monic potential $(1/2)\mu\omega_x^2 x^2$ and $(1/2)\mu\omega_y^2 y^2$, respectively. The frequency ω_x yields then an effective dot size $L_x=\sqrt{\hbar/\mu\omega_x}$, and similarly for L_y. The solution of the problem (A8) is given by an expansion in terms of the noninteracting system basis,

$$\Theta_m(\boldsymbol{\rho})=\sum_{n_x,n_y} a_{n_x,n_y}\varphi_{n_x}(x)\varphi_{n_y}(y), \qquad (A9)$$

$\varphi_n(x)$ being the solution of the harmonic oscillator Hamiltonian similar to Eq. (A6). The eigenfunctions Θ_m and relative exciton energies E_m are obtained as in Ref. 15 by a numerical diagonalization technique of the resulting Hamiltonian matrix (A8). Hence, geometrical confinement effects on excitons in quantum disk with elliptical cross section are studied following this matrix diagonalization approach, including the utilization of an optimized basis for larger dot diameters.[15]

4. Three-dimensional Coulomb correction

If the 3D exciton Bohr radius a_B is considerably larger than the QD height L_z $(a_B\gg L_z)$, the Z-axis confinement is stronger than the XY direction. Hence, the 3D Coulomb interaction effect on the exciton relative energy E_m can be treated by perturbation theory by

$$H_p=-\frac{e^2}{\varepsilon}\{[|\boldsymbol{\rho}_e-\boldsymbol{\rho}_h|^2+(z_e-z_h)^2]^{-1/2}-|\boldsymbol{\rho}_e-\boldsymbol{\rho}_h|^{-1}\},$$

as in Eq. (13). For $a_B\gg L_z$, the electron-hole pair mean value along the Z axis is smaller than the mean electron-hole separation $r_s=[\langle m||\boldsymbol{\rho}_e-\boldsymbol{\rho}_h|^2|m\rangle]^{1/2}$. Correspondingly, the excitonic correction energy up to first order can be written approximately as

$$\Delta E_m(n_e,n_h)\cong-\frac{e^2}{\varepsilon\sqrt{\langle m|(\boldsymbol{\rho}_e-\boldsymbol{\rho}_h)^2|m\rangle}}\left\langle n_e,n_h\left|\left(1+\frac{(z_e-z_h)^2}{\langle m|(\boldsymbol{\rho}_e-\boldsymbol{\rho}_h)^2|m\rangle}\right)^{-1/2}-1\right|n_h,n_e\right\rangle, \qquad (A10)$$

$$\cong-\frac{e^2}{\varepsilon\,r_s(m)}\left\langle n_e,n_h\left|\left(1-\frac{(z_e-z_h)^2}{2r_s^2}+\cdots\right)-1\right|n_h,n_e\right\rangle. \qquad (A11)$$

In Eq. (A10) the XY exciton coordinate has been substituted by its motion projection onto the well plane. The correction ΔE_m for a given excitonic state $|m\rangle$ depends on electron and hole subbands n_e and n_h and Eq. (A11) is cast into

$$\Delta E_m(n_e,n_h)\cong\frac{e^2}{2\varepsilon r_s^3(m)}[\langle n_e|z_e^2|n_e\rangle+\langle n_h|z_h^2|n_h\rangle+\cdots], \qquad (A12)$$

where

$$\langle n|z^2|n\rangle=L_z^2\left(\frac{1}{2}\left(\bar{k}_B^{-3}+\bar{k}_B^{-2}+\frac{\bar{k}_B^{-1}}{2}\right)+\frac{1}{4}\left\{\frac{1}{6}\left[1+\left(\frac{m_A\bar{k}_B}{m_B\bar{k}_A}\right)^2\right]-\frac{1}{\bar{k}_A^2}\left[\left(\frac{m_A\bar{k}_B}{m_B\bar{k}_A}\right)^2-1\right]+\frac{2}{\bar{k}_A^3}\left(\frac{\bar{k}_A}{2}-1\right)\frac{m_A\bar{k}_B}{m_B\bar{k}_A}\right\}\right)$$

$$\times\left[\frac{1}{\bar{k}_B}+\frac{1}{\bar{k}_A}\frac{m_A\bar{k}_B}{m_B\bar{k}_A}+\frac{1}{2}\left(\frac{m_A\bar{k}_B}{m_B\bar{k}_A}\right)^2+\frac{1}{2}\right]^{-1/2} \qquad (A13)$$

with $\bar{k}=kL_z$. These expressions are illustrated in Fig. 2 in the text.

[1] P. M. Petroff and G. Medeiros-Ribeiro, Mater. Res. Bull. **21**, 50 (1996).

[2] M. Fricke, A. Lorke, J. P. Kotthaus, G. Medeiros-Ribeiro, and P. M. Petroff, Europhys. Lett. **36**, 197 (1996).

[3] M. Grundmann, J. Christen, N. N. Ledentsov, J. Böhrer, D. Bimberg, S. S. Ruvimov, P. Werner, U. Richter, U. Gösele, J. Heydenreich, V. M. Ustinov, A. Yu. Egorov, A. E. Zhukov, P. S. Kop'ev, and Zh. I. Alferov, Phys. Rev. Lett. **74**, 4043 (1995).

[4] B. R. Bennett, B. V. Shanabrook, and R. Magno, Appl. Phys. Lett. **68**, 958 (1996).

[5] Yu. A. Pusep, G. Zanelatto, S. W. da Silva, J. C. Galzerani, P. P. Gonzalez-Borrero. A. I. Toropov, and P. Basmaji, Phys. Rev. B **58**, R1770 (1998).

[6] A. A. Sirenko, M. K. Zundel, T. Ruf, K. Eberl, and M. Cardona, Phys. Rev. B **58**, 12 633 (1998).

[7] P. Hawrylak, M. Potemski, D. J. Lockwood, H. J. Labbe, H. Kamada, H. Weman, J. Temmyo, and T. Tamamura, Physica E **2**, 652 (1998).

[8] M. Cardona, in *Light Scattering in Solids II*, edited by M. Cardona and G. Güntherodt, Topics in Applied Physics Vol. 50 (Springer, Berlin, 1982), p. 19.

[9] A. Cantarero, C. Trallero-Giner, and M. Cardona, Phys. Rev. B **39**, 8388 (1989).

[10] A. K. Ganguly and J. L. Birman, Phys. Rev. **162**, 806 (1967).

[11] R. J. Elliot, Phys. Rev. **108**, 1384 (1957).

[12] A. K. Sood, J. Menendez, M. Cardona, and K. Ploog, Phys. Rev. Lett. **54**, 2111 (1985); **54**, 2115 (1985).

[13] C. Trallero-Giner and F. Comas, Phys. Rev. B **37**, 4583 (1988).

[14] C. Trallero-Giner, R. Pérez-Alvarez, and F. García-Moliner, *Long-wave Polar Modes in Semiconductor Heterostructures* (Pergamon, New York, 1998).

[15] J. Song and S. E. Ulloa, Phys. Rev. B **52**, 9015 (1995).

[16] C. Trallero-Giner, A. Cantarero, and M. Cardona, Phys. Rev. B **40**, 4030 (1998).

[17] G. Bastard, *Wave Mechanics Applied to Heterostructures* (Les Éditions de Physique, Paris, 1988).

[18] M. Strassburg, V. Kutzer, U. W. Pohl, A. Hoffmann, I. Broser, N. N. Ledentsov, D. Bimberg, A. Rosenauer, U. Fischer, D. Gerthsen, I. L. Krestnikov, M. V. Maximov, P. S. Kop'ev, and Zh. I. Alferov, Appl. Phys. Lett. **72**, 942 (1998).

[19] M. Y. Shen, T. Goto, E. Kurts, Z. Zhu, and T. Yao, J. Phys.: Condens. Matter **10**, L171 (1998).

[20] J. Nieto-Jalil and R. Pérez-Alvarez, Phys. Status Solidi A **164**, 699 (1997).

[21] H. Rho, H. E. Jackson, S. Lee, M. Dobrowolska, and J. K. Furdyna (unpublished), reported the LO phonon in CdSe dots at $\simeq 22/cm^{-1}$.

[22] M. Abramowitz and I. A. Stegun, *Handbook of Mathematical Functions* (U.S. GPO, Washington, D.C., 1964).

[23] *Landolt-Börnstein Tables*, edited by O. Madelung, H. Schulz, and H. Weiss (Springer, Berlin, 1982), Vols. III/17a and 22a.

[24] C. Trallero-Giner, A. Debernardi, M. Cardona, E. Menéndez-Proupin, and A. I. Ekimov, Phys. Rev. B **57**, 4664 (1998).

[25] K. W. Böer, *Survey of Semiconductor Physics* (Van Nostrand Reinhold, New York, 1990).

[26] U. E. Laheld and G. T. Einevoll, Phys. Rev. B **55**, 5184 (1997).